Received: 3 August 2017 | Accepted: 15 November 2017

DOI: 10.1111/jace.15352

ORIGINAL ARTICLE

Journal of the American Ceramic Society

Melter feed viscosity during conversion to glass: Comparison between low-activity waste and high-level waste feeds

Tongan Jin[1] | **Jaehun Chun**[1] | **Derek R. Dixon**[1] | **Dongsang Kim**[1] | **Jarrod V. Crum**[1] | **Charles C. Bonham**[1] | **Bradley J. VanderVeer**[1] | **Carmen P. Rodriguez**[1] | **Brigitte L. Weese**[1] | **Michael J. Schweiger**[1] | **Albert A. Kruger**[2] | **Pavel Hrma**[1]

[1]Pacific Northwest National Laboratory, Richland, Washington

[2]U.S. Department of Energy, Office of River Protection, Richland, Washington

Correspondence
Tongan Jin, Pacific Northwest National Laboratory, Richland, WA.
Email: tongan.jin@pnnl.gov

Funding information
U.S. Department of Energy (DOE) Waste Treatment and Immobilization Plant Project

Abstract

During nuclear waste vitrification, a melter feed (a slurry mixture of a nuclear waste and various glass forming and modifying additives) is charged into the melter where undissolved refractory constituents are suspended together with evolved gas bubbles from complex reactions. Knowledge of flow properties of various reacting melter feeds is necessary to understand their unique feed-to-glass conversion processes occurring within a floating layer of melter feed called a cold cap. The viscosity of two low-activity waste (LAW) melter feeds were studied during heating and correlated with volume fractions of undissolved solid phase and gas phase. In contrast to the high-level waste (HLW) melter feed, the effects of undissolved solid and gas phases play comparable roles and are required to represent the viscosity of LAW melter feeds. This study can help bring physical insights to feed viscosity of reacting melter feeds with different compositions and foaming behavior in nuclear waste vitrification.

KEYWORDS
foaming, nuclear waste feed, undissolved solids, viscosity

1 | INTRODUCTION

The U.S. Department of Energy currently has about 210 000 m^3 radioactive waste stored in underground tanks at the Hanford Site in southeastern Washington. They plan to vitrify this waste into glass in the Hanford Tank Waste Treatment and Immobilization Plant (WTP), which involves the separation of the wastes into high-volume/low-activity waste (LAW) and low-volume/high-level waste (HLW). While the majority of radioactivity (~95%) is contained in the HLW, approximately 90% of the waste volume has been characterized as LAW. The waste itself, composed of 40-60 elements, exists as water-soluble salts and sludge.[1-3]

In the nuclear waste glass processing, the feed (a slurry mixture of waste with glass-forming and modifying additives) is continuously charged onto the cold cap (a floating layer of melter feed on top of a pool of molten glass) that covers 90%-95% of the melt surface in a continuous electrical glass-melting furnace (i.e., a melter). The melter feed moves through the cold cap and undergoes chemical reactions and phase transitions until it is converted to molten glass.[4-8] A feed-to-glass conversion over a wide range of temperatures (from ~100°C to ~1100°C) involves the formation of molten salts that react with feed solids, intermediate products, and ultimately the glass-forming melt. Evolved gases from such complex reactions escape through open pores in the cold cap until ~700°C-800°C, but a fraction of residual gases can be trapped in the transient melt (i.e., high alkaline borate amorphous melt phase in the early melting stage while silica and other minerals have not been completely dissolved).[9-11] These foams in the cold cap reduce the heat transfer from molten glass into the reacting feed, which can significantly decrease the rate of

melting.[12] This transient melt also contains various solid particles, both dissolving and precipitating.

Understanding the physical and mechanical properties of the melter feed in its final stage of conversion to molten glass is crucial for both feed formulation and modeling of the feed-to-glass conversion. Modeling of the feed viscosity in the cold cap based on the data from small-scale experiments is an essential part of the cold-cap model development for the WTP project. In small-scale melter tests, viscosity and foaming behaviors have been measured to develop the mathematical model of the cold cap structure as well as other aspects of the feed-to-glass conversion such as foaming.[12] The model is expected to predict melter operation parameters. One of the key parameters is the melting rate, or rate of glass production during vitrification in the melter which will greatly impact the cost and schedule of the entire WTP project. Another example is the melter off-gas emissions. The melter off-gas consists predominantly water vapor, evolved gases such as CO_2 and NO_2, and minor volatile species such as B, Na, K, technetium-99 (^{99}Tc), and cesium-137 (^{137}Cs). The volatile radionuclides ^{99}Tc and ^{137}Cs in the off-gas stream are the major technical challenge of designing the off-gas recycling system. It has been demonstrated that with a larger cold cap coverage of the melter surface area, volatile loss of ^{99}Tc is decreased.[13,14]

Studies on viscosity have been extensively focused on the glass (prepared from melter feeds) and corresponding models as a function of temperature and compositions,[15-19] although several attempts to correlate foaming with transient melt viscosity have been made.[20,21] In a previous study[22] important physico-chemical changes (e.g., dissolution of solids, gas evolution, and feed mass) over various temperatures were correlated with feed viscosity of a high-alumina, simulated HLW feed (called A0), by combining various analytical techniques such as thermogravimetric analysis (TGA), gas pycnometry, feed volume expansion tests, and a custom-made high-temperature viscometer. This analysis indicated that the effects of undissolved solids (i.e., quartz for that case) and the effect of gases could not be distinguished because the quartz fraction and bubble fraction happened to be linearly dependent.

While the majority of the waste volume is associated with LAW, only rheological properties of different LAW feed slurries have been studied thus far.[23] Understanding the viscosity of LAW melter feeds during the final stages of the melter conversion process represents the first step in understanding melter feed rheology from drying to full glass conversion. Unlike typical HLW feeds, LAW feeds contain a high level of sodium salts (e.g., sodium nitrates/nitrites/carbonates),[24,25] which implies that qualitatively different rheology would result from different foaming behavior associated with the appreciable amount of evolved gases. A comparative study[3] with LAW melter feeds provided insights into understanding the flow properties for a wide range of reacting melter feeds (e.g., melter feeds with different foaming behavior). Two simulated LAW feeds, AN-102 and AZ-102 (representing LAW feeds formulated based on waste streams with different sodium/nitrate concentrations) were initially selected for tests on a scaled melter system.[24,25] Chemical analysis results of these reacting feeds[3] demonstrated that different compositions of the salt phase and transient melt phase between these two feeds could significantly impact the feed-to-glass conversion reactions such as dissolving of minerals and volatilization of radioactive ^{99}Tc. The compositional impact on rheological behaviors of LAW feeds, which has not been investigated, is also essential for understanding the overall melting process.

In this work, the viscosities of two representative simulated LAW melter feeds, AN-102 and AZ-102 were studied during the feed-to-glass conversion. Variations of gas and undissolved solids associated with the conversion process were analyzed and employed as the key variables. A comparison between the LAW feeds and the high-alumina, HLW feed was made to comprehend differences between feeds with different natures. The following section explains the basic concepts of viscosity modeling of the feed-to-glass conversion. Section 3 introduces the experimental methods and approach used to analyze relevant physico-chemical changes and their effects on feed viscosity. Sections 4 and 5 describe the results and discusses these results.

2 | BACKGROUND OF MODEL DEVELOPMENT

Melter feeds with on-going feed-to-glass conversion are far from a dilute suspension. The foaming layer of the cold cap contains up to 80 vol% gas bubbles; and in the remaining transient melt (volume of bubbles excluded), there is up to 25 vol% of undissolved solids. Various studies on viscosity of dense suspensions[26,27] have been extensively performed. However, the highly complex nature of the reacting feeds prevents a simple application of equations proposed for suspensions with higher volume fractions of suspending entities (e.g., solids and gases) such as the Krieger-Dougherty equation.[27] Therefore, a different type of relationship between viscosity and suspended entities is needed.

The following relationship for reacting feed viscosity (η_F), has been previously introduced[22]

$$\log \frac{\eta_F}{\eta_M} = f_0 + f_s \varphi_s + f_g \varphi_g \quad (1)$$

where φ_s and φ_g are the volume fractions of undissolved solids and gas phase (porosity), respectively, and η_M is the viscosity of transient melt which corresponds to that of "continuous" phase surrounding undissolved solids and gas

in the reacting feed. In Equation (1), the η_F/η_M ratio is analogous to a relative viscosity (but with on-going feed-to-glass conversion) of which many studies on viscosity of colloidal suspension have been focused.[26,27] Two coefficients, f_s and f_g, represent the effects of undissolved solids and gas on the melting feed viscosity and f_0 is the coefficient accounting for other effects such as the presence of tiny crystals, local compositional inhomogeneity connected with a dissolution process of silica and other solids in a transient melt, and the non-uniform temperature field in the sample. While the tiny crystals might impact the behavior of bubbles (e.g., bubble coalescence[28,29]), no direct interference was assumed via a linear superposition. Hereafter, subsections will show subsequent experimental details with relations to obtain necessary information to understand the viscosity of reacting feeds based on Equation (1).

Although the experimental procedures to determine the factors in Equation (1) of the LAW and HLW feeds were similar; the volume fractions (φ_s and φ_g) of LAW required more complicated analysis. Furthermore, the undissolved solid phase of HLW A0 feed was mostly identified as quartz during the viscosity measurement at 750°C to 1200°C. In contrast, there were several different undissolved solid phases in the LAW feeds during melting up to between 1000°C and 1100°C. Therefore, a quantitative X-ray diffraction (XRD) analysis of the two LAW feeds, AN-102 and AZ-102, was performed to determine crystalline phases and their volume fractions in the samples (see Sections 3.2 and 3.3).

3 | EXPERIMENTAL PROCEDURE

3.1 | Feeds preparation

Tables 1 and 2 show the three simulated melter feed compositions used in this study, AN-102 (high-nitrate), AZ-102 (low-nitrate), and A0 (high-alumina HLW). The A0 glass feed was originally designed for the WTP with waste loading of ~45% and then formulated and simplified to vitrify a high-alumina high-level waste.[30] The three feeds were formulated to vitrify corresponding wastes to produce AN-102 glass (designated as LAWE7H), AZ-102 glass (LAWE10H),[3,24,25] and high alumina HLW glass (designated as A0)[31], respectively. Chemicals of the "Simulated LAW" were added to deionized (DI) water and were fully dissolved. The chemicals and minerals of the "Additives" were then added to the simulated waste to prepare the slurry feeds (equivalent to a "glass batch" in commercial glass production). Slurry feeds were thoroughly mixed and dried at 105°C for 12 hours to obtain the feeds used in the tests described below. Slurry-batching was similarly employed to prepare A0 samples. The slurry feed was prepared, dried, crushed into powder, and placed in an oven at 105°C overnight.

3.2 | Quantitative XRD analysis

The purpose of quantitative XRD was to obtain the mass fraction of crystalline phases (undissolved solids) and the amorphous phase (transient melt) in the reacting feed.[3,32,33] Small aliquots (~20 g) of powdered feed were packed into separate platinum crucibles and placed into a furnace at room temperature. The samples were thermally treated at 5°C·min^{-1} up to 1100°C with individual samples removed at selected temperatures starting at 700°C. The samples were ground into fine powders and doped with 5 wt% CaF_2 as an internal standard before being analyzed by XRD with a Bruker D8 Advance (Bruker AXS Inc., Madison, WI, USA) instrument equipped with a CuK_α target of 40 kV and 40 mA. The instrument had a LynxEye position-sensitive detector with a scan range of 3°-75° 2θ. Scan parameters used for sample analysis were 5°-75° 2θ with a step of 0.015° 2θ and a 2.5-second dwell at each step. TOPAS (Bruker AXS Inc.) software was used to identify and quantify the crystal phases based on the internal standard.

3.3 | Material density and bulk density

As stated in Section 2, volume fractions of the undissolved solids and the gas phase are key parameters of the model shown in Equation (1). Densities of each phase and density of the overall reacting feed were needed to obtain the volume fractions:

$$\rho = \sum \rho_i \varphi_i \tag{2}$$

where ρ is the average density, and ρ_i and φ_i are the ith phase constituent density and volume fraction, respectively.

To calculate the average density, the material density (ρ_c), defined as the density of the condensed phases (i.e., the averaged density of the mixture of the transient melt and the undissolved solid inclusions), and bulk density (ρ_b), defined as the average density of the continuous phase including the trapped gas bubbles, are desired. The material density of each finely ground, thermally treated feed sample, prepared as described in Section 3.2 in order to carefully remove existing voids in the samples, was measured by a Micromeritics AccuPyc II 1340 gas pycnometer (Micromeritics Instrument Corporation, Norcross, GA, USA). To measure the bulk density of the samples, mass and volume of feeds were measured as functions of temperature. The volume expansion test (as shown in Figure 1) was employed to observe change in the relative volume of dried feeds during 5°C·min^{-1} of heating from room temperature to 1100°C as described by Henager et al[34] The expansion of dried feed was profiled by image analysis to obtain the normalized bulk volume ($V(T)$ / V_0) where $V(T)$ is the volume at temperature T and V_0 is the volume at room temperature, as explained in

TABLE 1 Batch compositions of AN-102, AZ-102, and A0 melter feeds ($g \cdot kg^{-1}$ Glass)[3,22]

Component Simulated LAW + Additives	AN-102	AZ-102	A0 Slurry feed components[a]	
$Al(NO_3)_3 \cdot 9H_2O$	76.81	1.22	$Al(OH)_3$	367.50
H_3BO_3	0.09	–	H_3BO_3	269.83
$Ca(NO_3)_2 \cdot 4H_2O$	1.27	–	CaO	60.80
$Na_2CrO_4 \cdot 4H_2O$	2.41	2.42	Na_2CrO_4	11.13
KOH	6.44	6.43	KNO_3	3.03
NaOH	46.17	2.21	NaOH	99.53
NiO	0.08	0.08	$NiCO_3$	6.33
PbO	0.08	0.08	$Pb(NO_3)_2$	6.17
SiO_2	0.09	0.26		
NaCl	3.25	3.25		
NaF	1.72	1.72	NaF	14.73
$Na_3PO_4 \cdot 12H_2O$	6.60	6.56	$Fe(H_2PO_2)_3$	12.43
Na_2SO_4	10.54	14.20	Na_2SO_4	3.57
$NaNO_2$	56.58	24.81	$NaNO_2$	3.40
$NaNO_3$	82.64	6.76		
Na_2CO_3	42.97	28.62		
Sodium formate ($NaHCO_2$)	21.74	–		
Sodium oxalate ($Na_2C_2O_4$)	1.26	–	$Na_2C_2O_4 \cdot 3H_2O$	1.30
Glycolate ($C_2H_4O_3$)	26.72	–		
Citric acid ($C_6H_8O_7$)	7.84	–		
Oxalic acid ($C_2H_2O_4 \cdot 2H_2O$)	–	2.24		
Re_2O_7	0.01	0.01		
			$Bi(OH)_3$	12.80
Additives				
Kyanite (Al_2SiO_5)	86.20	104.59		
H_3BO_3	175.13	176.73		
Wollanstonite ($CaSiO_3$)	135.78	150.49		
Hematite (Fe_2O_3)	51.92	50.10	$Fe(OH)_3$	73.83
Li_2CO_3	78.47	105.44	Li_2CO_3	88.30
Olivine (Mg_2SiO_4)	31.03	61.23	$Mg(OH)_2$	1.70
Na_2CO_3		23.77		
Quartz (SiO_2)	316.35	329.94	SiO_2	305.03
Rutile (TiO_2)	13.29	13.15		
Zincite (ZnO)	34.60	34.80	$Zn(NO_3)_2 \cdot 4H_2O$	2.67
Zircon ($ZrSiO_4$)	44.38	44.83	$Zr(OH)_4 \cdot 0.654H_2O$	5.50
Total dry feed mass[b] (g)	1362.46	1195.94		1349.60
Target glass mass (g)	1000.00	1000.00		1000.00
Calculated mass loss[c]	26.6%	16.4%		25.9%

"–" indicates zero value.

[a]The A0 feed has been simplified based on the original composition[30,31]; the chemical forms of the HLW components have been modified; and the additives (with ~0.45 waste loading) consist of H_3BO_3, CaO, Li_2CO_3, NaOH, and SiO_2.

[b]Sum of all simulated waste chemicals plus additives excluding water added to make the slurry.

[c]A difference between the total dry mass of feed components and target glass mass divided by the total dry mass of feed components.

TABLE 2 Glass Compositions of AN-102, AZ-102, and A0[3,22]

Component (mass fraction)	AN-102	AZ-102	A0
Al_2O_3	0.0602	0.0607	0.2407
B_2O_3	0.0986	0.0994	0.1522
Bi_2O_3	–	–	0.0115
CaO	0.0631	0.0696	0.0609
Cr_2O_3	0.0008	0.0008	0.0052
Fe_2O_3	0.0543	0.0548	0.0592
K_2O	0.0054	0.0054	0.0014
Li_2O	0.0317	0.0426	0.0358
MgO	0.0149	0.0294	0.0012
Na_2O	0.1352	0.0572	0.0961
NiO	0.0001	0.0001	0.0040
PbO	0.0001	0.0001	0.0041
SiO_2	0.4472	0.4889	0.3057
TiO_2	0.0138	0.0139	–
ZnO	0.0346	0.0348	0.0008
ZrO_2	0.0296	0.0299	0.0040
Cl	0.0020	0.0020	–
F	0.0008	0.0008	0.0067
P_2O_5	0.0012	0.0012	0.0106
SO_3	0.0065	0.0086	–
SUM	1.0000	1.0000	1.0000
Waste loading[a]	0.1622	0.0620	~0.45

"–" indicates zero value.

[a]Waste loading is the mass fraction of oxides and halogens contributed by the waste to the glass.

recent work,[35] and subsequently the bulk density was simply calculated by $\rho_b(T) = m(T)/V(T)$, where m is the sample mass at temperature T as measured by the quantitative XRD (Section 3.2).

3.4 | Viscosity of reacting feeds

Figure 2 provides a schematic diagram of the experimental setup for the viscosity measurement. Approximately 125 g samples of powder feed were poured into a platinum crucible containing the viscometer spindle set at 0.5 cm from the bottom of the crucible inside the furnace. The sample was then heated at 5°C·min^{-1} from room temperature to 1100°C. The measurement started when the instrument thermocouple reached between 700°C and 750°C (when the viscosity decreased to lower than approximately 10^4 Pa·s, which is the physical limit of spindle rotation). The spindle was rotated with an increasing speed as temperature increased, typically up to ~160 rpm at 1100°C. Torques were converted into viscosities via spindle factor as described in the previous work.[22] For each feed, the temperature-viscosity curve was averaged by three measurements under the same conditions.

The possible shear rate in our study was limited by foaming and torque limit. In the lower temperature region (i.e., ~800°C-900°C), the shear rate was limited due to the maximum torque allowed for the measurements. Measurements at different shear rates (up to ~2.7 s^{-1}) indicated that the variation in viscosity was not appreciable in the measurements with such limitations.

Slip conditions in a fluid with high undissolved solid content cause an issue when performing rheological measurements using a rotating spindle. This is due to the displacement of suspending particles/bubbles away from the smooth wall potentially causing a solvent-rich layer to develop near the rotating inner cylinder.[36] However, rough surfaces for both the crucible and spindle used in our measurements were expected to reduce the slip appreciably, as previously reported,[37] though it cannot be completely eliminated.

4 | RESULTS

As shown in Figure 2, the melter feed during the feed-to-glass conversion consists of three different phases, the transient melt, undissolved solids (assuming the different undissolved solids as one phase because they are indistinguishable in the viscosity model), and gas phase (bubbles), which are listed in Table 3. In order to develop the

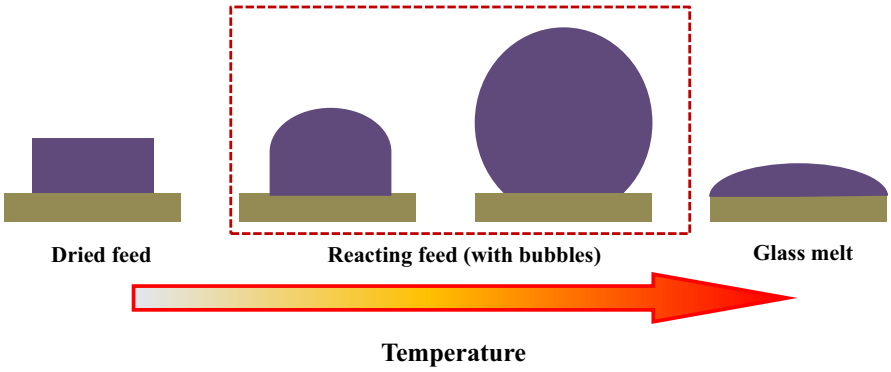

FIGURE 1 Schematic drawings of the volume expansion test

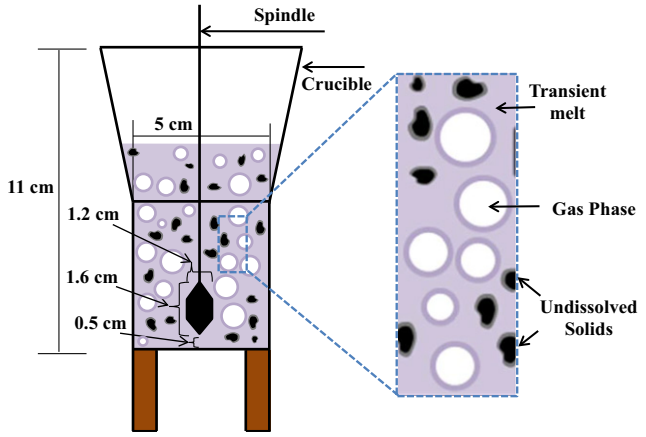

FIGURE 2 Schematic drawings of the viscosity measurement of the reacting feeds

viscosity model (based on Equation (1) in Section 2), the volume fraction and viscosity of each individual phase was measured as described in Section 3.

Table 3 summarizes the methods used to obtain parameters of each phase for the viscosity model. Viscosities and volume fractions of each phase were obtained by measurements, calculations, or reasonable approximations for the model. The viscosity of the transient melt phase, $\eta_M(T)$, is obtained from a glass composition-viscosity empirical model (Sections 4.1 and 4.4). The volume fractions of different phases can be obtained by combining the composition analysis (i.e., quantitative XRD), the density measurement, and the volume expansion measurement (Sections 4.1-4.3). Finally, the directly measured viscosity of the reacting feed will be shown in Section 4.5.

4.1 | Composition analysis

Compositions of the transient melt and undissolved solids were measured to obtain the volume fractions of each. Quantitative XRD analysis gave the mass fractions of detected crystal phases (Table 4). Accordingly, the mass fraction of the transient melt (w_M), i.e., the amorphous phase in the analyzed sample was calculated by $w_M = 1 - \sum_{j=1}^{9} w_j$, where w_j is the j-th crystal mass fraction and subscript M stands for melt. As shown in Table 4, nine original crystalline phases have been identified in the temperature range of interest, ≥750°C: quartz, rutile, hematite, zircon, kyanite, wollastonite, olivine, zincite, and diopside. Most of these were crystal phases in the original batch and dissolved into the transient melt during the heating. Diopside, $CaMgSi_2O_6$, was an intermediate phase formed between 800°C and 1000°C,[38-41] which was not one of the original crystal phases. Beside these phases, other identifiable phases were sodium nitrate, nosean, and lithium silicate. However, those phases did not remain solid in the temperature range of interest.

Compositions of the transient melts (Table 5) were calculated using the formula:

$$F_{i,M} = \frac{F_i - \sum_{j=1}^{N=9} F_{ij} w_j}{w_M} \quad (3)$$

where $F_{i,M}$ is the i-th component mass fraction (j = Al_2O_3, B_2O_3, CaO, Fe_2O_3, K_2O, Li_2O, MgO, Na_2O, SiO_2, TiO_2, ZnO, ZrO_2, and SO_3) in transient melt, F_i is the i-th component mass fraction in the glass (Table 2), and F_{ij} is the i-th component mass fraction in the j-th crystal phase.

4.2 | Volume fraction of transient melt and undissolved solids

Volume fractions of the amorphous phase (i.e., the transient melt), φ'_M, and crystal phases (i.e., undissolved solids), φ'_s, were calculated based on the mass fractions and densities listed in Table 4 using the formulas:

$$\varphi'_M = 1 - \rho_c \sum_{j=1}^{N=9} \frac{w_j}{\rho_j} \quad (4)$$

TABLE 3 Methods to obtain the parameters associated with each phase in a reacting feed

Phase	Composition $F_i(T)$	Density ρ[a]	Viscosity η(T)	Volume fraction φ(T)
Undissolved solids (subscript **s**)	Known compositions of mineral additives	Literature density of the mineral additives	+∞ as a reasonable approximation	Calculated by density and mass fraction measured by quantitative XRD
Transient melt (subscript **M**)	Calculated by target glass composition and quantitative XRD results of mineral additives	Calculated by material density (measured) and densities of mineral additives (literature)	Calculated by an empirical composition-viscosity model	Calculated by density and mass fraction measured by quantitative XRD
Gas (bubbles) (subscript **g**)	Not needed	Neglected as a reasonable approximation	Neglected as a reasonable approximation	Measured by volume expansion test

[a]Densities of the mineral additives are considered as constants with negligible thermal expansion with elevated temperature.

TABLE 4 Densities (ρ_j) and mass fractions of the crystal phases and the amorphous phase (w_j)

Phase name	Density, ρ_j ($g \cdot cm^{-3}$)[38-41]	AN-102, w_j					AZ-102, w_j				
		700°C	800°C	900°C	1000°C	1100°C	700°C	800°C	900°C	1000°C	1100°C
Quartz (SiO_2)	2.65	0.0387	0.0113	–	–	–	0.155	0.0529	0.0143	–	–
Rutile (TiO_2)	4.26	0.002	–	–	–	–	0.007	0.0074	0.0041	–	–
Hematite (Fe_2O_3)	5.18	–	–	–	–	–	0.018	–	–	–	–
Zircon ($ZrSiO_4$)	4.6	0.0248	0.0169	0.0056	0.0015	–	0.0295	0.0244	0.02	0.0105	0.0038
Kyanite (Al_2SiO_5)	3.25	0.03	0.0153	–	–	–	0.0668	0.0246	–	–	–
Wollanstonite ($CaSiO_3$)	2.9	0.0375	0.0288	–	–	–	0.0644	0.0228	0.0129	0.0089	–
Olivine (Mg_2SiO_4)	3.58	0.0012	–	–	–	–	0.0328	0.0107	0.005	–	–
Zincite (ZnO)	5.67	–	–	–	–	–	0.0014	–	–	–	–
Diopside ($CaMgSi_2O_6$)	3.31	–	–	–	–	–	–	0.1196	0.0684	0.0065	-
Amorphous	$\rho_M(T)$[a]	0.8659	0.9276	0.9944	0.9985	1.0000	0.6251	0.7376	0.8753	0.9741	0.9962
Total		1.00	1.00	1.00	1.00	1.00	1.00	1.00	1.00	1.00	1.00

"–" indicates zero value.

[a]$\rho_M(T)$ is temperature dependent, calculated by Equation (8) in Section 4.2.

$$\varphi'_s = 1 - \varphi'_M \tag{5}$$

where w_j is the j-th crystal mass fraction, ρ_j is the j-th phase density, and ρ_c is the material density (Section 3.3). Note that φ'_M and φ'_s are volume fractions in total condensed phases (transient melt and undissolved solids, i.e., $\varphi'_s + \varphi'_M = 1$). Hence, φ'_s is different from the φ_s in Equation (1). The spatial volume fractions (including gas phase) should satisfy $\varphi_s + \varphi_M + \varphi_g = 1$ and thus are given by:

$$\varphi_M = \varphi'_M(1 - \varphi_g) \tag{6}$$

$$\varphi_s = \varphi'_s(1 - \varphi_g) \tag{7}$$

The density values were used without considering thermal expansion. The density of the transient melt, ρ_M, was calculated as:

$$\rho_M = \frac{w_M}{\frac{1}{\rho_c} - \sum_{j=1}^{N=9} \frac{w_j}{\rho_j}} \tag{8}$$

Figure 3 shows the volume fractions of undissolved solids for the three feeds, along with cubic-interpolated data between the measurement intervals of 100°C. The

TABLE 5 Compositions (mass fraction, x_i)[a] of the amorphous phases vs temperature

	AN-102					AZ-102				
	700°C	800°C	900°C	1000°C	1100°C	700°C	800°C	900°C	1000°C	1100°C
Al_2O_3	0.080	0.051	0.056	0.056	0.056	0.042	0.064	0.069	0.063	0.062
B_2O_3	0.070	0.103	0.095	0.095	0.094	0.161	0.133	0.112	0.101	0.097
CaO	0.056	0.052	0.061	0.062	0.062	0.065	0.034	0.052	0.066	0.071
Fe_2O_3	0.072	0.059	0.055	0.056	0.055	0.056	0.082	0.067	0.061	0.058
K_2O	0.005	0.006	0.006	0.005	0.006	0.009	0.007	0.006	0.005	0.005
Li_2O	0.028	0.034	0.032	0.031	0.032	0.071	0.060	0.052	0.045	0.044
MgO	0.021	0.018	0.017	0.016	0.016	0.001	0.000	0.015	0.031	0.032
Na_2O	0.108	0.148	0.139	0.135	0.138	0.097	0.080	0.071	0.061	0.060
SiO_2	0.472	0.457	0.462	0.464	0.461	0.399	0.454	0.478	0.488	0.489
SO_3	0.001	0.005	0.005	0.005	0.006	0.009	0.009	0.008	0.007	0.007
TiO_2	0.021	0.014	0.013	0.013	0.013	0.018	0.013	0.013	0.014	0.014
ZnO	0.046	0.038	0.036	0.035	0.035	0.059	0.050	0.041	0.037	0.036
ZrO_2	0.019	0.016	0.024	0.027	0.028	0.012	0.015	0.016	0.021	0.025

[a]The mass fraction x_i represents the oxide component mass fraction in the amorphous phase.

undissolved solid phase consists of only quartz in the A0 HLW feed but several minerals in the AN-102 and AZ-102 LAW feeds, as listed in Table 4. The quartz in A0 HLW feed (15% at 800°C) gradually dissolves with a fraction of a percent remaining at 1100°C. In AZ-102 feed, the 20% undissolved solids at 800°C, the highest content of the three feeds, drops to less than 5% at 1000°C, nearly the same as quartz in A0 feed. In contrast, AN-102 feed has only ~5% undissolved solids at 800°C, which are completely dissolved by 900°C.

4.3 | Volume fraction of evolved gasses

Figure 4A shows volume changes of volume expansion tests with temperature. The A0 feed started to shrink slightly at 700°C-900°C and slightly expanded over 900°C due to foaming.[22] In contrast, LAW feeds showed significant volume expansion. This is due to a large amount of evolved gases in the transient melt that connects at 600°C-700°C. The evolved gases were mainly from carbonates in the feed (with contributions from nitrates and nitrites). The maximum volumes of AN-102 and AZ-102 feeds became ~8 times and ~3 times of their original volumes, respectively. Significant foaming of the two LAW feeds occurred between 600°C and 900°C followed by a minor expansion above 900°C.

The volume fraction of evolved gas, or porosity, can be obtained from a combination of the volume expansion test and density measurement as described by the following relation:

$$\varphi_g(T) = \frac{\rho_c(T) - \rho_b(T)}{\rho_c(T) - \rho_g(T)} \cong 1 - \frac{\rho_b(T)}{\rho_c(T)} = 1 - \left(\frac{m(T)}{m_0}\right)\left(\frac{V_0}{V(T)}\right)\frac{\rho_{b,0}}{\rho_c(T)} \quad (9)$$

where ρ_g is the gas density, ρ_b is the bulk density, and ρ_c is the material density defined in Section 3.3. Note that $\rho_g \ll \rho_c$ is used as a reasonable approximation in Equation (9). Here, $m(T)$ is the sample mass at a given temperature T, $V(T)$ is the sample volume at T, and subscript 0 indicates room temperature.

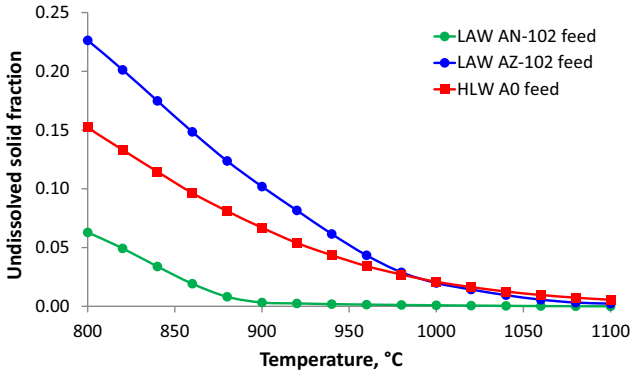

FIGURE 3 Volume fractions of the undissolved solid phase

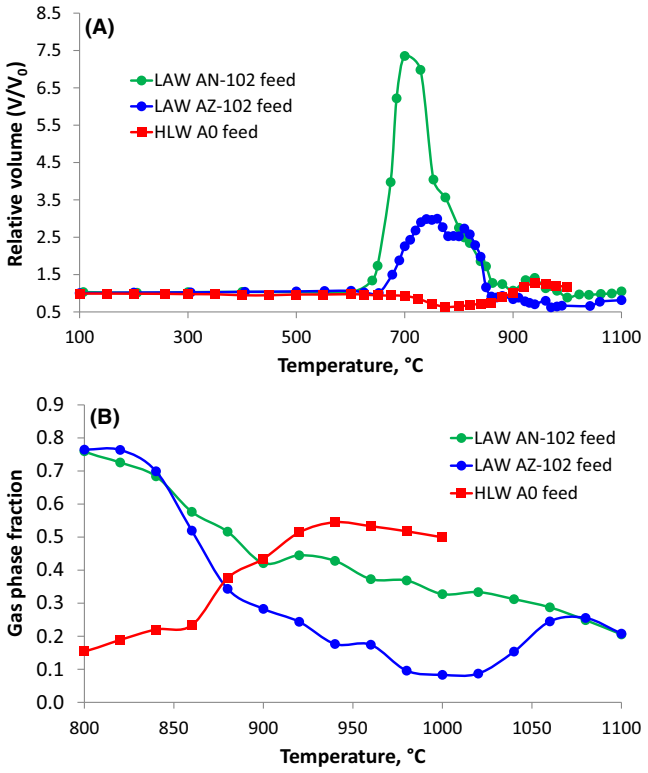

FIGURE 4 Volume expansion of the feeds (A) and volume fractions (B) of the gas phase in the reacting feeds as functions of temperature

Figure 4B shows φ_g at $T > 800$°C. At temperatures below 800°C, the transient melts of HLW and LAW feeds were not continuously connected and the viscosity could not be measured. Therefore, as mentioned before, the model was fit to data at temperatures >800°C. The volume fraction of gas phase in the A0 HLW feed gradually increased from 0.15 at 800°C to 0.5 at 930°C and then began to decrease. The volume fractions of gas phase of the AN-102 and AZ-102 feeds were ~0.75 at 800°C and decreased to about 0.2 at 1100°C. The gas volume fraction of AZ-102 decreased to a minimum value of ~0.1 at 1000°C and increased to ~0.2 from 1000°C to 1100°C. The volume expansion data over 1000°C of the HLW A0 feed is not shown because the model fitting for this feed did not include temperature range over 1000°C.[22] For the LAW feeds, the temperature was expanded to 1100°C.

4.4 | Viscosity of transient melt

The viscosity of transient melt (η_M) was obtained via modeling. The model used an Arrhenius equation to define the relationship between viscosity and temperature:

$$\ln \eta = A + \frac{1}{T}\sum_{i=1}^{N} B_i x_i \quad (10)$$

where A is a composition-independent pre-exponential factor, T (°C) is the temperature of the transient melt or glass melt, N is the total number of components in the glass, B_i is the i-th component coefficient, and x_i is the i-th oxide component mass fraction. The B_i values can be found in Hrma et al[17].

The composition of the transient melt from 700°C to 1100°C was determined as described in Section 3.1 and listed in Table 5. The calculated viscosities of transient melts and final glass melts using Equation (10) are plotted in Figure 5. The formulated composition of glass (Table 2) was used. The transient melts have lower viscosities for both feeds because they contain higher fractions of Na_2O and B_2O_3. For AN-102, the two viscosity curves reach a similar value over 900°C when the minerals are nearly dissolved, which can be indicated by nearly zero mass fractions of crystalline phases. The two viscosity curves of AZ-102 are almost identical at a higher temperature (i.e., around 1000°C), which can be similarly understood. Note that for HLW A0, the transient melt viscosity and the glass viscosity became identical at about 1100°C.[22]

4.5 | Viscosity of reacting feeds

Figure 6 shows measured viscosities of the feeds by the viscometer. The viscosity of the HLW A0 melter feed has been reported previously.[22] The viscosity measurements are reproducible considering uncertainties and unavoidable inhomogeneity of the sample during conversion from feeds to glass; uncertainties of the measurements (three replicates for each sample) were less than 10%. As mentioned, the aim of this work was to develop a model based on Equation (1) which correlates the viscosity-temperature functions to key variables such as the composition-dependent transient melt viscosity (η_M) and the volume fractions of undissolved solids and bubbles (φ_s and φ_g). In the temperature range of 800°C-1100°C, the feed viscosity (η_F) of the HLW A0 feed drops from $10^{3.1}$ to $10^{0.9}$ Pa·s, for AZ-102 feed from $10^{3.4}$ to $10^{0.9}$ Pa·s, and for AZ-102 from $10^{2.8}$ to $10^{0.5}$ Pa·s.

5 | DISCUSSION

5.1 | Comparison of different viscosities

Figure 7 compares the temperature-viscosity curves of the feed, the transient melt, and the final glass. As expected, feed viscosity is higher than that of the transient melt. The effects of the bubbles and the undissolved solids are major factors to be quantified and discussed in the next section. The transient melt viscosity and the final glass viscosity match at high temperatures, but this is not necessarily the case for the feed viscosity even though the composition is the same as the final glass composition. The three curves all match at ~1000°C for AN-102 but the feed viscosity of AZ-102 has a higher viscosity in the final glass. Although uncertainties associated with the experiments (e.g., non-uniform temperature distribution[22] and other experimental errors) and the empirical model for the transient melt/glass viscosity could be responsible, the silica-rich inhomogeneity is the likely cause due to the significant effect of silica on viscosity, especially considering the late disappearance of solids in AZ-102 (Figure 7).

5.2 | Feed viscosity model: effects of the undissolved solid phase and gas bubbles

Table 6 lists the model coefficients obtained by fitting Equation (1) to the data, i.e., the volume fractions of the undissolved solid and the gas phases ($\varphi_s(T)$ and $\varphi_g(T)$) (Sections 3.2 and 3.3) and the viscosities of the transient melt and the feed ($\eta_M(T)$ *and* $\eta_F(T)$), using the least

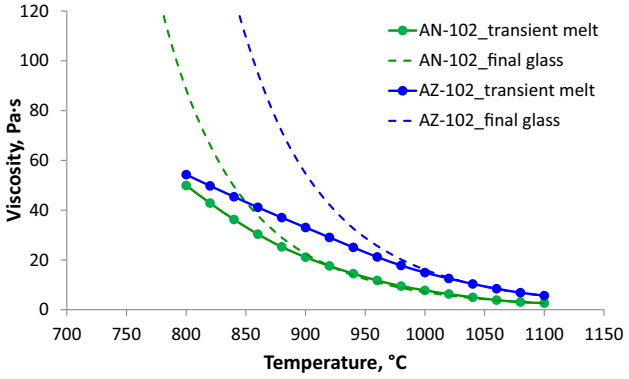

FIGURE 5 Viscosities of the transient melt and the final glass melt of the AN-102 and AZ-102 LAW feeds

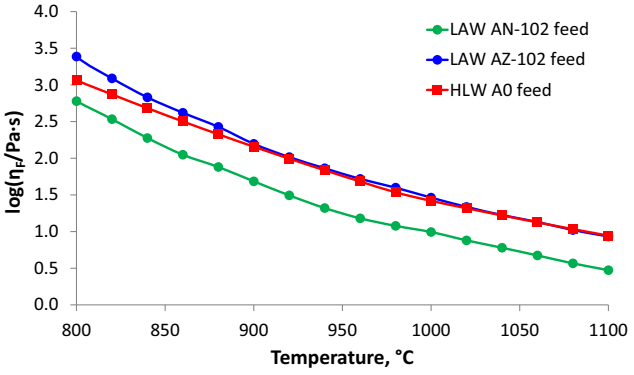

FIGURE 6 Viscosity of reacting feeds

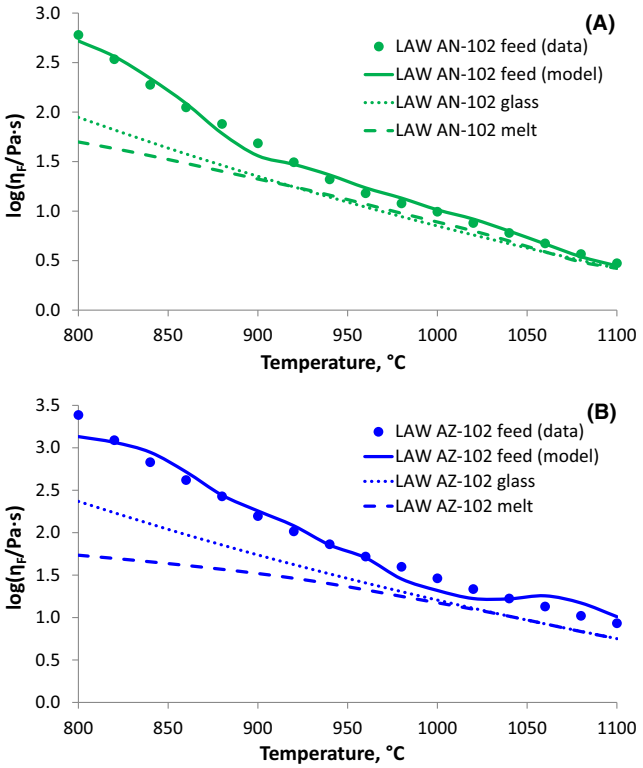

FIGURE 7 Comparison of measured/model-predicted feed viscosities, estimated glass viscosities, and estimated transient melt viscosities

TABLE 6 Model fitting coefficients

	A0 ($T \leq 980°C$)	A0 ($T > 980°C$)		AN-102	AZ-102
f_0	−0.058	0.068	f_0	−0.1084	−0.0957
f_{sg}	8.822	3.141	f_g	0.5716	1.5782
			f_s	45.0120	5.1140

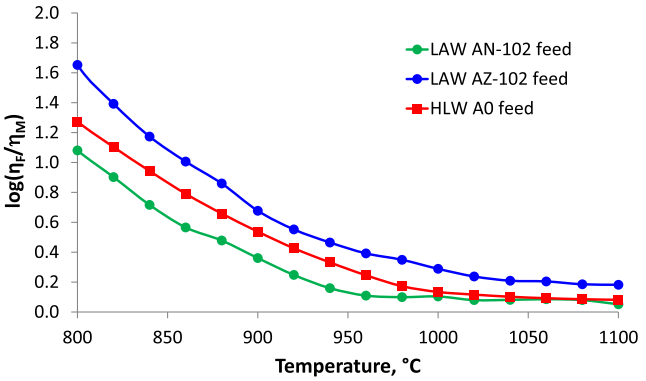

FIGURE 8 Relative feed viscosity η_F/η_M

squares method. Figure 8 presents the relative feed viscosity as a function of temperature ($\eta_M(T)$ *and* $\eta_F(T)$).

For A0, the volume fractions of the reacting feed, $\varphi_s(T)$ / $\varphi_g(T)$, were correlated, and the f_s and f_g coefficients could not be determined independently. Instead of Equation (1), the relationship $\log(\eta_F/\eta_M) = f_0 + f_{sg}\varphi_s$ was fitted to data obtaining f_0 and f_{sg} values for two temperature ranges at $T \leq 980°C$ and $T > 980°C$. This is based on an assumption that the silica-rich layers around dissolving quartz grains exist at $T \leq 980°C$ but become connected to form a high-viscosity network of silica-rich inhomogeneity at $T > 980°C$[22] resulting in the negative f_0 (less viscous) and positive f_0 (more viscous) values, respectively. As shown previously,[42,43] SiO_2 diffusing into the melt from dissolving quartz grains was initially accumulated in the diffusion layers at the solid-melt interfaces. As a result, viscosity of the transient melt remained low until the diffusion layers impinged on each other while the SiO_2 concentration in the melt became gradually uniform. This explains the transition from the negative f_0 at $T \leq 980°C$ to positive values at $T > 980°C$ in the A0 feed.[22]

No such correlation occurred in the two LAW feeds. The dissolving solids in AN-102 and AZ-102 feeds consisted of quartz (SiO_2), zircon ($ZrSiO_4$), kyanite (Al_2SiO_5), wollastonite ($CaSiO_3$), and other minerals listed in Table 4. The negative f_0 coefficients indicate the presence of a connected low-viscosity network in the transient melts while the viscosity increasing components (SiO_2, Al_2O_3, and ZrO_2) remained concentrated in the diffusion layers around the dissolving particles.

As indicated by the coefficients, the effect of the undissolved solid phase (f_s) would be more significant than that of the gas phase (f_g), although the effect of the evolved gas phase would still be appreciable. As shown in Figures 7 and 8, the AN-102 feed (i.e., high volume of gas and low volume of undissolved solids) has a low relative feed viscosity (η_F / η_M). Although fractions of undissolved solids and bubbles for the two LAW feeds and HLW are very different, the difference in a normalized or relative feed viscosity (η_F / η_M) is insignificant.

Previous studies[44,45] indicated that an effective viscosity of bubble suspensions varied with the volume fraction of gas. At a small capillary number (Ca) (i.e., (Ca $\ll$ 1), the effective viscosity increases with the volume fraction, but it decreases with the volume fraction at large Ca (i.e., Ca $\gg$ 1). Here, the capillary number is defined by:

$$\mathrm{Ca} = \frac{\eta_M r \dot{\gamma}}{\Gamma} \tag{11}$$

where η_M is the viscosity of transient melt, r is the radius of the undeformed bubble, $\dot{\gamma}$ is the shear rate, and Γ is the surface tension.[44]

During the feed-to-glass transition process, the bubble size (in radius, r) could be estimated as smaller than 0.004 m based on X-ray tomography[46] and the surface tension could be estimated as 0.3 $N \cdot m^{-1}$.[47] Using the shear

rate calculated based on our experimental set up (max. 2.7 s^{-1}) and viscosity of the transient melt (as shown in Figure 5), a maximum capillary number would be ~0.1 which implies that bubbles are not deformable and thus the effective viscosity increases with the volume fraction. This would be qualitatively consistent with the positive f_g values in our study.

Modeling of the feed rheological behavior is an essential part of the on-going work to develop a comprehensive model of the cold cap to predict the melting rate as a function of feed properties and melter conditions. Furthermore, this approach can be used to explore a correlation between the effects of different types of additives[48] and the viscosity model fitting coefficients.

6 | CONCLUSIONS

A combination of various measurements, such as pellet expansion tests, pycnometry, and XRD analysis, are necessary to obtain the melter feed viscosity as a function of the feed-to-melt conversion process. In spite of complexities such as dispersed dissolving solids and gas bubbles, ongoing compositional changes, and continuously increasing temperature, the melter feed viscosity can be described by a simple model.

Generally, for all studied HLW and LAW feeds, the undissolved solid phase in the glass-forming melt strongly increases the feed viscosity while the evolved gas phase has a moderate increasing effect. The LAW feeds, release a large amount of evolved gas compared to HLW feeds. Therefore, foaming influences the LAW feed viscosity, especially at temperatures <900°C. A comparative study using the LAW and HLW melter feeds performed in this work provide a key element for the development of the cold-cap model applicable for feeds with different compositions and foaming behaviors.

ACKNOWLEDGMENTS

The authors gratefully acknowledge the financial support provided by the U.S. Department of Energy Waste Treatment and Immobilization Plant Project. Pacific Northwest National Laboratory is operated by Battelle for DOE under contract DE-AC05-76RL01830. We are grateful to Renee Russell and Will Eaton of Pacific Northwest National Laboratory for insightful suggestions.

ORCID

Tongan Jin http://orcid.org/0000-0002-2216-5311
Jaehun Chun http://orcid.org/0000-0002-2291-6496
Dongsang Kim http://orcid.org/0000-0002-3669-9154
Albert A. Kruger http://orcid.org/0000-0001-8468-0813

REFERENCES

1. U.S Department of Energy. River protection project system plan. Report No.: ORP-11242, Rev. 7. Richland, WA, 2014.
2. Kim D. Glass property models, constraints, and formulation approaches for vitrification of high-level nuclear wastes at the US Hanford Site. *J Korean Ceram Soc*. 2015;52:90-92.
3. Jin T, Kim D, Tucker AE, et al. Reactions during melting of low-activity waste glasses and their effects on the retention of rhenium as a surrogate for technetium-99. *J Non-Cryst Solids*. 2015;425:28-45.
4. Hrma P, Kruger AA. Nuclear waste glasses: continuous melting and bulk vitrification. Proceedings of 9th European Society of Glass (ESG) Conference with the Annual Meeting of the International Commission on Glass (ICG). Trencin, Czech Republic, 2008.
5. Hrma P, Kruger AA, Pokorný R. Nuclear waste vitrification efficiency: cold cap reactions. *J Non-Cryst Solids*. 2012;358:3559-3562.
6. Pokorný R, Pierce DA, Hrma P. Melting of glass batch: model for multiple overlapping gas-evolving reactions. *Thermochim Acta*. 2012;541:8-14.
7. Pokorný R, Hrma P. Model for the conversion of nuclear waste melter feed to glass. *J Nucl Mater*. 2014;445:190-199.
8. Dixon DR, Schweiger MJ, Riley BJ, et al. Temperature distribution within a cold cap during nuclear waste vitrification. *Environ Sci Technol*. 2015;49:8856-8863.
9. Matyáš J, Hrma PR, Kim D-S. *Melt Rate Improvement for High-Level Waste Glass*. PNNL-14003. Pacific Northwest National Laboratory. Richland, WA, 2002.
10. Hrma P, Schweiger MJ, Humrickhouse CJ, et al. Effect of glass-batch makeup on the melting process. *Ceram-Silik*. 2010;54:193-211.
11. Rodriguez CP, Chun J, Schweiger MJ, et al. Application of evolved gas analysis to cold-cap reactions of melter feeds for nuclear waste vitrification. *Thermochim Acta*. 2014;592:86-92.
12. Pokorný R, Hilliard ZJ, Dixon DR, et al. One-dimensional cold cap model for melters with bubblers. *J Am Ceram Soc*. 2015;98:3112-3118.
13. Bibler NE, Fellinger TL, Marra SL, et al. Tc-99 and Cs-137 Volatility from the DWPF Production Melter During Vitrification of the First Macrobatch of HLW Sludge at the Savannah River Site. *MRS Proc*. 1999;608:697-702.
14. Zamecnik JR, Crawford CL. *Offgas Emissions from the Vitrification of Hanford Envelope C Low Activity Waste*. WSRC-MS-2003-00072, Rev. 0. Aiken, SC: Savannah River Technology Center and Westinghouse Savannah River Company, LLC; 2003.
15. Hrma P. Glass viscosity as a function of temperature and composition: a model based on Adam-Gibbs equation. *J Non-Cryst Solids*. 2008;354:3389-3399.
16. Hrma P. Arrhenius model for high-temperature glass-viscosity with a constant pre-exponential factor. *J Non-Cryst Solids*. 2008;354:1962-1968.
17. Hrma P, Arrigoni BM, Schweiger MJ. Viscosity of many-component glasses. *J Non-Cryst Solids*. 2009;355:891-902.

18. Hrma P, Han S-S. Effect of glass composition on activation energy of viscosity in glass-melting-temperature range. *J Non-Cryst Solids*. 2012;358:1818-1829.
19. Hrma P, Kruger AA. High-temperature viscosity of many-component glass melts. *J Non-Cryst Solids*. 2016;437:17-25.
20. van der Schaaf J, Beerkens RGC. A model for foam formation, stability, and breakdown in glass-melting furnaces. *J Colloid Interface Sci*. 2006;295:218-229.
21. Hrma P. Effect of heating rate on glass foaming: transition to bulk foam. *J Non-Cryst Solids*. 2009;355:257-263.
22. Marcial J, Chun J, Hrma P, et al. Effect of Bubbles and Silica Dissolution on Melter Feed Rheology during Conversion to Glass. *Environ Sci Technol*. 2014;48:12173-12180.
23. Chun J, Oh T, Luna M, et al. Effect of particle size distribution on slurry rheology: nuclear waste simulant slurries. *Colloid Surf A-Physicochem Eng Asp*. 2011;384:304-310.
24. Matlack KS, Muller IS, Pegg IL, et al. *Improved Technetium Retention in Hanford LAW Glass – Phase 1*. VSL-10R1920-1. Washington, DC: Vitreous State Laboratory, The Catholic University of America; 2010.
25. Matlack KS, Muller IS, Callow RA, et al. *Improved Technetium Retention in Hanford LAW glass – Phase 2*. VSL-101R2260-1. Washington, DC: Vitreous State Laboratory, The Catholic University of America; 2011.
26. Russel WB, Saville DA, Schowalter WR. *Colloidal Dispersions*. New York: Cambridge University Press; 1989.
27. Hiemenz PC, Rajagopalan R. *Principles of Colloid and Surface Chemistry*, 3rd edn. New York: Marcel Dekker Inc.; 1997.
28. Stevenson P. *Foam Engineering: Fundamentals and Applications*. Singapore: John Wiley & Sons; 2012.
29. Berg JC. *An Introduction to Interfaces & Colloids: The Bridge to Nanoscience*. Hackensack, NJ: World Scientific Publishing Co.; 2010.
30. Matlack KS, Gan H, Gong W, et al. *High Level Waste Vitrification System Improvements*. VSL-07R1010-1 Rev 0. Washington, DC: Vitreous State Laboratory, The Catholic University of America; 2007.
31. Hrma PR, Schweiger MJ, Arrigoni BM, et al. *Effect of Melter-Feed-Makeup on Vitrification Process*. ORP-42728-FP Revision 0. Richland, WA: Pacific Northwest National Laboratory; 2009.
32. Xu K, Hrma P, Rice J, et al. Melter feed reactions at T ≤ 700°C for nuclear waste vitrification. *J Am Ceram Soc*. 2015;98:3105-3111.
33. Xu K, Hrma P, Rice JA, et al. Conversion of nuclear waste to molten glass: cold-cap reactions in crucible tests. *J Am Ceram Soc*. 2016;99:2964-2970.
34. Henager SH, Hrma P, Swearingen KJ, et al. Conversion of batch to molten glass, I: volume expansion. *J Non-Cryst Solids*. 2011;357:829-835.
35. Hilliard Z, Hrma P. A method for determining bulk density, material density, and porosity of melter feed during nuclear waste vitrification. *J Am Ceram Soc*. 2016;99:98-105.
36. Chun JH, Poloski AP, Hansen EK. Stabilization and control of rheological properties of Fe_2O_3/$Al(OH)_3$-rich colloidal slurries under high ionic strength and pH. *J Colloid Interface Sci*. 2010;348:280-288.
37. Barnes HA. A review of the slip (wall depletion) of polymer-solutions, emulsions and particle suspensions in viscometers - its cause, character, and cure. *J Non-Newton Fluid Mech*. 1995;56:221-251.
38. Yaws' Critical Property Data for Chemical Engineers and Chemists [Internet]. Knovel. 2012, 2013, 2014. Available from: http://app.knovel.com/hotlink/toc/id:kpYCPDCECD/yaws-critical-property/yaws-critical-property.
39. Knovel Critical Tables (2nd Edition) [Internet]. Knovel. 2008. Available from: http://app.knovel.com/hotlink/toc/id:kpKCTE000X/knovel-critical-tables/knovel-critical-tables.
40. Yaws' Thermophysical Properties of Chemicals and Hydrocarbons (Electronic Edition) [Internet]. Knovel. 2010. Available from: http://app.knovel.com/hotlink/toc/id:kpYTPCHE02/yaws-thermophysical-properties/yaws-thermophysical-properties.
41. Mavko G, Mukerji T, Dvorkin J. *The Rock Physics Handbook: Tools for Seismic Analysis of Porous Media*. Published Online: Cambridge University Press; 2003.
42. Schweiger MJ, Hrma P, Humrickhouse CJ, et al. Cluster formation of silica particles in glass batches during melting. *J Non-Cryst Solids*. 2010;356:1359-1367.
43. Pokorný R, Rice JA, Crum JV, et al. Kinetic model for quartz and spinel dissolution during melting of high-level-waste glass batch. *J Nucl Mater*. 2013;443:230-235.
44. Llewellin EW, Mader HM, Wilson SDR. The rheology of a bubbly liquid. *Proc R Soc A-Math Phys Eng Sci*. 2002;458:987-1016.
45. Llewellin EW, Mader HM, Wilson SDR. The constitutive equation and flow dynamics of bubbly magmas. *Geophys Res Lett*. 2002;29: 23-1-23-4.
46. Harris WH, Guillen DP, Klouzek J, et al. X-ray tomography of feed-to-glass transition of simulated borosilicate waste glasses. *J Am Ceram Soc*. 2017;100:3883-3894.
47. Pokorný R, Hrma P. Mathematical modeling of cold cap. *J Nucl Mater*. 2012;429:245-256.
48. Lee S, VanderVeer BJ, Hrma P, et al. Effects of heating rate, quartz particle size, viscosity, and form of glass additives on high-level waste melter feed volume expansion. *J Am Ceram Soc*. 2017;100:583-591.

How to cite this article: Jin T, Chun J, Dixon DR, et al. Melter feed viscosity during conversion to glass: Comparison between low-activity waste and high-level waste feeds. *J Am Ceram Soc*. 2017;00:1-12. https://doi.org/10.1111/jace.15352